Available online at www.sciencedirect.com
ScienceDirect
Journal of Solid State Chemistry 181 (2008) 253–262
JOURNAL OF SOLID STATE CHEMISTRY
www.elsevier.com/locate/jssc

Phase stability and ionic conductivity in substituted $La_2W_2O_9$

D. Marrero-López*, J. Peña-Martínez, J.C. Ruiz-Morales, P. Núñez*

Departamento de Química Inorgánica, Universidad de La Laguna, Avda. Astrofísico Francisco Sánchez s/n, 38200-La Laguna, Tenerife, Spain

Received 11 October 2007; received in revised form 21 November 2007; accepted 27 November 2007
Available online 27 December 2007

Abstract

Different substitutions, i.e. Sr^{2+}, Ba^{2+}, K^{+}, Nb^{5+} and V^{5+}, have been performed in the triclinic α-$La_2W_2O_9$ structure in order to stabilise the high temperature and better ionic conductor cubic β-phase. This approach has been used to try to obtain a new series of ionic conductors with LAMOX-type structure without molybdenum and presumably better redox stability compared to β-$La_2Mo_2O_9$. Nanocrystalline materials obtained by a freeze-drying precursor method at 600 °C exhibit mainly the β-$La_2W_2O_9$ structure, however, the triclinic α-form is stabilised as the firing temperature increases and the crystallite size grows. Only high levels of Ba^{2+} and V^{5+} substitutions retained the cubic form at room temperature after firing above 1100 °C. However, these phases are metastable above 700 °C, exhibiting an irreversible transformation to the low temperature triclinic α-phase. The synthesis, structure, phase stability, kinetic of phase transformation and electrical conductivity of these materials have been studied in the present report.

Keywords: $La_2Mo_2O_9$; Solid electrolyte; Nanocrystalline materials; Phase transition

1. Introduction

In recent years there has been a growing interest in phases derived from $La_2Mo_2O_9$, the so-called LAMOX compounds [1–3]. Such compounds possess high oxide ion conductivity at intermediate temperatures and comparable to doped ceria [4]. Hence, they have potential electrochemical applications, such as oxygen sensors, dense ceramic membranes for oxygen separation, oxygen pumps and fuel cells components [5,6]. Non-substituted $La_2Mo_2O_9$ exhibits two different crystallographic polymorphs, α and β, with a reversible structural phase transition at 560 °C associated with long-range oxygen vacancy ordering [2,3]. The high temperature β-polymorph is a better conductor than the low temperature α-polymorph and it crystallises in a cubic symmetry (s.g. $P2_13$) [2]. On the other hand, the α-polymorph is an ordered superstructure relative to the more symmetric β-form with a slight monoclinic distortion (s.g. $P2_1$) [7].

The main limitations for practical applications of non-substituted $La_2Mo_2O_9$ as solid electrolyte are the phase transition and low stability under reducing conditions. The phase transition produces a drastic drop in the conductivity below 560 °C and possibly mechanical failure due to the high thermal expansion of the unit cell volume between the high and low temperature polymorphs. A wide range of substitutions have been investigated in order to stabilise the β-polymorph, such as: La^{3+} by Bi^{3+} [8], Ca^{2+} [9,10], Ba^{2+} [10–12], K^{+} [12,13], Y^{3+} [14] and rare earth elements [15–17], whereas Mo^{6+} has been substituted by Nb^{5+} [18,19], V^{5+}, Fe^{3+}, Al^{3+} [20], Cr^{6+} [21] and W^{6+} [21–26]. Most of these substitutions stabilise the β-polymorph at room temperature, although generally they do not improve the ionic conductivity. In addition, β-$La_2Mo_2O_9$ exhibits also a limited stability range under reducing conditions due to the presence of Mo^{6+}, which is partially reduced to lower oxidation states, increasing the non-desirable n-type electronic conductivity and phase degradation [27–29]. The redox stability of $La_2Mo_2O_9$-based materials can be improved by partial substitution of Mo^{6+} by W^{6+} [24–26]. The similar ionic radius of Mo^{6+} and W^{6+}, 0.59 and 0.60 Å, respectively, permits high levels of substitution, up to 80% [22], maintaining the cubic β-$La_2Mo_2O_9$

*Corresponding authors. Fax: +34 922318461.
E-mail addresses: damarre@ull.es (D. Marrero-López), pnunez@ull.es (P. Núñez).

0022-4596/$ - see front matter © 2007 Elsevier Inc. All rights reserved.
doi:10.1016/j.jssc.2007.11.024

structure and the high ionic conductivity, typically $0.1\,S\,cm^{-1}$ at 750 °C [25], whereas a triclinic phase isostructural with α-$La_2W_2O_9$ is stabilised at higher W contents [30]. The better redox stability of $La_2Mo_{2-y}W_yO_9$ series seems to be explained by the lower reducibility of W^{6+} in comparison to Mo^{6+}. Indeed, XPS studies confirmed that tungsten is not reduced during the phase decomposition under highly reducing conditions [31,32]. Nevertheless, a low level of tungsten substitution as 25% improves significantly the redox stability of these compounds.

The corresponding lanthanum tungstate, $La_2W_2O_9$ with triclinic structure at room temperature, also exhibits a reversible phase transition at 1070 °C [33]. The high temperature β-$La_2W_2O_9$ polymorph is suspected to be cubic with a crystal structure similar to that of β-$La_2Mo_2O_9$, although it has not been corroborated by a structural study. One could expect that the introduction of suitable dopants in the lanthanum and/or tungsten site of α-$La_2W_2O_9$ might stabilise the high temperature β-$La_2W_2O_9$ polymorph, allowing obtaining a new series of ionic conductors with high ionic conductivity and presumably better redox stability compared to the stabilised β-$La_2Mo_2O_9$. In this context, we have studied different substitutions, $La_{2-x}A_xW_{2-y}B_yO_{9-\delta}$ ($A = Sr^{2+}$, Ba^{2+}, K^+ and $B = Nb^{5+}$, V^{5+}), in order to stabilise the cubic phase at room temperature and to evaluate the transport properties and stability of these new materials.

2. Experimental

2.1. Synthesis

Nanocrystalline materials of $La_{2-x}A_xW_{2-y}B_yO_{9-\delta}$ ($A = Sr^{2+}$, Ba^{2+}, K^+ and $B = Nb^{5+}$, V^{5+}) series were prepared from a freeze-drying precursor method, following a similar procedure than that previously described in several reports [34–36]. Materials used as reagents were La_2O_3 (99.99%), WO_3 (99.8%), $Sr(NO_3)_2$ (99.9%), $Ba(NO_3)_2$ (99.9%), K_2CO_3 (99.9%), $NbCl_5$ (99.5%) and V_2O_5 (99.5%), all of them supplied from Aldrich. La_2O_3 was precalcined at 1000 °C for 2 h to achieve dehydration and decarbonation. Metal nitrates, which are generally hygroscopic, were previously studied by thermogravimetric analysis up to 1000 °C in a Perkin-Elmer TG/DTA instrument (mod. Pyris Diamond) for determining the accurate cation content in the original metal nitrates from the corresponding stable oxides. Stoichiometric amounts of La_2O_3 and WO_3 were dissolved in hot diluted nitric acid and ammonia, respectively, whereas the metal nitrates were dissolved in distilled water. Ethylenediaminetetraacetic acid (EDTA) (99.5% Aldrich) was used as complexing agent in a molar ratio ligand:metal 1:1. $NbCl_5$ was dissolved separately in ethanol and then EDTA and ammonia solutions were added. This solution was slowly heated in a hot plate to evaporate the ethanol. The different cation solutions were mixed and stirred for 15 min, resulting in a homogeneous and transparent solution. The pH was adjusted to 9 by ammonia addition. A typical preparation of 100 ml gives rise to approximately 3 g of final oxide. Droplets of these solutions were flash frozen in liquid nitrogen retaining the homogeneity of the original solution. The frozen droplets were dehydrated by vacuum sublimation at a pressure of 1–10 Pa in a Heto Lyolab 3000 freeze dryer during 2 days. In this way, dried solid precursors were obtained. The precursor powders were initially calcined at 300 °C to produce the organic matter pyrolysis. Then, they were ground and calcined again at 600 °C for 3 h to remove the residual organic species and to achieve crystallisation of the compounds. The powder samples were pressed into pellets and fired between 950 and 1300 °C for 3 h and then slowly cooled to room temperature. The tungsten oxide losses during the sintering were considered negligible. Finally, the pellets were finely ground and characterised by several techniques. The samples are hereafter labelled as LMO for $La_2Mo_2O_9$, LWO for $La_2W_2O_9$, and A_x and B_y for $La_{2-x}A_xW_{2-y}B_yO_{9-\delta}$ series, respectively.

2.2. Powders characterisation

X-ray diffraction (XRD) patterns were recorded using a Philips X'Pert Pro diffractometer, equipped with a Ge(1 1 1) primary monochromator and a X'Celerator detector. The scans were collected in the 2θ range (5–100°) with 0.016° step for 2 h. Structure refinements were performed using the FullProf and WinPlotr softwares [37,38].

Thermogravimetric and differential thermal analysis curves (TG/DTA) were recorded with a Perkin-Elmer instrument (Pyris Diamond) at a heating/cooling rate of $10\,°C\,min^{-1}$ under air atmosphere.

The morphology of the sintered pellets was monitored using a scanning electron microscope (SEM) (mod. Jeol LTD, JSM-6300). All preparations were covered with a thin film of sputtered gold for better image definition.

2.3. Electrical characterisation

Cylindrical disks of 10 and ~2 mm of diameter and thickness, respectively, were prepared pressing the nanocrystalline powders at 125 MPa. The resulting pellets were sintered in air at 1300 °C for 3 h, rendering relative densities higher than 99%. Pt-paste electrodes were deposited on each side of the pellet and then fired at 700 °C for 15 min. Impedance spectra were obtained using a frequency response analyser (Solartron 1260) in static air in the 0.1 Hz–1 MHz frequency range with an ac perturbation of 25 and 100 mV in the high and low temperature range, respectively. The spectra were acquired during the heating and cooling processes between 300 and 1200 °C with a stabilisation time of 30 min between consecutive measurements. Impedance spectra were analysed with ZView program [39]. The resistance and capacitance values of

the different contributions were obtained by fitting the impedance spectra data with equivalent circuits. The equivalent circuit used consists of (RQ) elements in series, where R is a resistance and Q is a pseudocapacitance in parallel.

3. Results and discussions

3.1. Phase formation and stability

The XRD patterns corresponding to the nanopowders of non-substituted and substituted $La_2W_2O_9$ series fired at 600 °C are displayed in Fig. 1. As can be observed the main diffraction peaks for nanocrystalline $La_2W_2O_9$ correspond to the high temperature cubic β-phase instead of the triclinic structure of the bulk phase. However, some Bragg reflections associated with the triclinic phase are also observed. The same behaviour has been observed in other systems. For example, the high temperature tetragonal phase of ZrO_2 becomes stable at room temperature when the particle size is less than 30 nm and above this critical size, tetragonal to monoclinic transformation occurs [40,41]. Hence, the stabilisation of the cubic form at room temperature for non-substituted $La_2W_2O_9$ can be associated to the nanocrystalline nature of the synthesised materials, where the cubic phase is eventually retained in a metastable state. In fact, the material reverts to the stable triclinic phase when the firing temperature increases above 700 °C and the crystallite size grows from 27 nm at 600 °C to 50 nm at 700 °C.

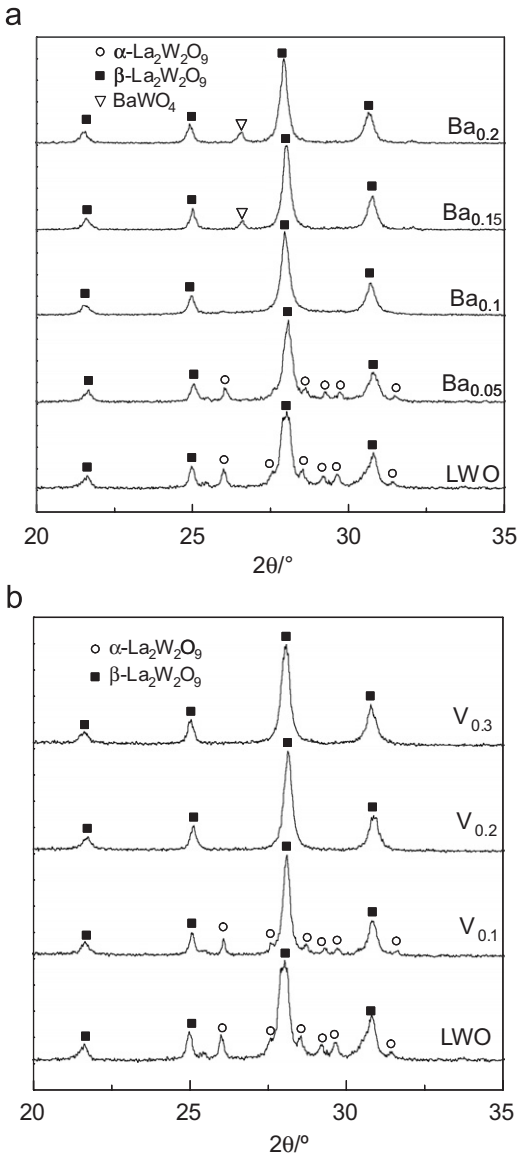

Fig. 1. XRD patterns for non-substituted $La_2W_2O_9$ (LWO) and (a) $La_{2-x}Ba_xW_2O_{9-\delta}$ (Ba_x) and (b) $La_2W_{2-y}V_yO_{9-\delta}$ (V_y) series calcined at 600 °C during 5 h.

The intensity of the diffraction peaks for the triclinic phase vanishes as the substitution of Ba^{2+} and V^{5+} increases, indicating total stabilisation of the cubic form. Nevertheless, a small fraction of scheelite $BaWO_4$ is observed for samples with high levels of Ba-substitution (Fig. 1a).

The XRD patterns for $Ba_{0.2}$ and $V_{0.3}$ samples fired between 600 and 1300 °C are shown in Fig. 2. In the case of $Ba_{0.2}$ (Fig. 2a), the cubic phase and a small fraction of $BaWO_4$ are observed at 600 °C. It should be noted that A(Mo,W)O_4 (A = Ba, Sr, Ca) phases are very stable at intermediate temperatures and they usually appear as impurities in compounds containing these elements [12]. Above 600 °C a gradual phase transformation occurs, coexisting three crystalline phases; the cubic and triclinic $La_2W_2O_9$ polymorphs and $BaWO_4$. Between 800 and 1000 °C the cubic phase is not detected; however, this is partially recovered after fired at 1100 °C, appearing a mixture of α- and β-polymorphs. Finally, the cubic phase is stabilised at room temperature when fired at 1300 °C. A similar trend is observed in V-substituted samples (Fig. 2b). In this case, the cubic form is retained in the nanocrystalline material up to 700 °C. A new crystalline phase appears at 800 °C, which was indexed to a monoclinic unit cell, similar to $Nd_2W_2O_9$ (PDF 023-1268). Then, a mixture of α- and β-polymorphs are observed again at 1000 °C. Finally, the cubic form is obtained at 1100 °C or higher firing temperature.

One can observe that the unit cell volume for nanocrystalline samples is somewhat higher than that of bulk crystal. For instance, the cell volume for $V_{0.3}$ decreases from 359.47 Å^3 at 600 °C to 358.12 Å^3 at 1300 °C. This is usually associated to lattice distortion in nanocrystalline materials due to superficial defects [41,42].

The phase transformation and segregation of impurities as the temperature increases in substituted LWO samples could be explained in terms of two factors; the thermal variation of both crystallite size and cation solubility. As previously mentioned, samples with crystallite size below 50 nm retained the high temperature cubic polymorph at room temperature in a metastable state and this is nearly independent on the substitution content. When the

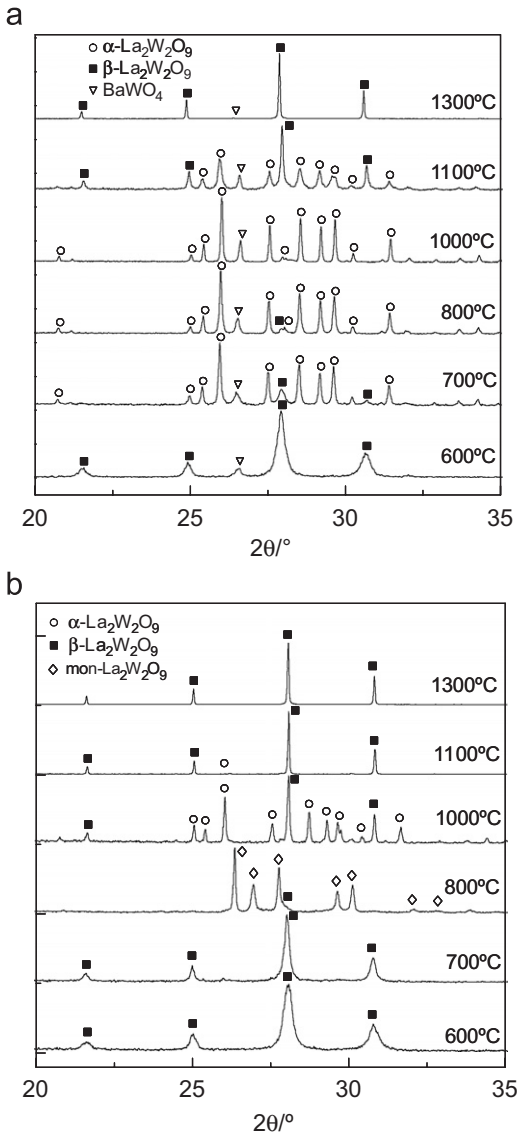

Fig. 2. XRD patterns for (a) $La_{1.8}Ba_{0.2}W_2O_{9-\delta}$ ($Ba_{0.2}$) and (b) $La_2W_{1.7}V_{0.3}O_{9-\delta}$ ($V_{0.3}$) phases as a function of the firing temperature. The different phases that appear as the temperature increases are also indicated in the figure.

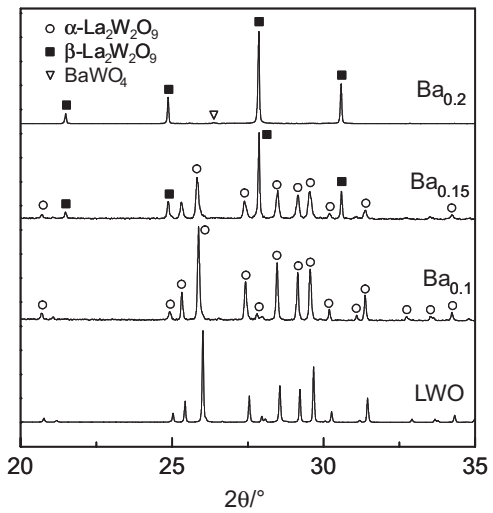

Fig. 3. XRD patterns for $La_{2-x}Ba_xW_2O_{9-\delta}$ (Ba_x) series calcined at 1300 °C as a function of the Ba content.

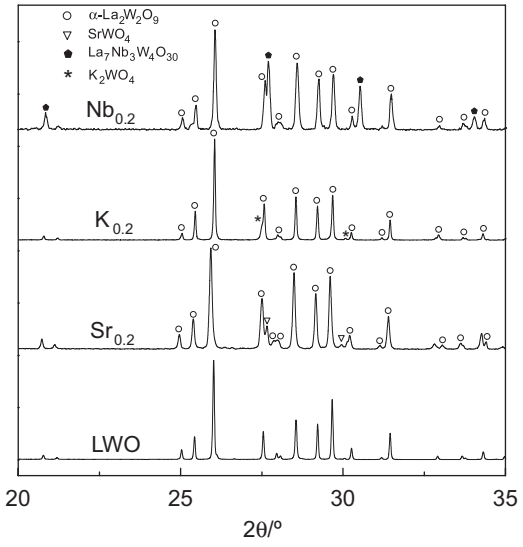

Fig. 4. XRD patterns for different cation substitutions in $La_2W_2O_9$ (i.e. Sr^{2+}, Nb^{5+} and K^+).

temperature increases, the crystal size grows and samples with low substitution recover the stable triclinic phase. In addition, it is well reported that the solubility of dopants is enhanced in nanocrystalline materials [41]. Thus, the segregations of $BaWO_4$ as the temperature increases in the intermediate temperature range could be associated to a decrease of the Ba-solubility with the increase of the crystallite size. Note that the fraction of $BaWO_4$ in Fig. 2a increases with the firing temperature between 700 and 1000 °C, confirming this hypothesis. In addition, the cation solubility increases with the firing temperature above 1000 °C and the cubic phase is stabilised at room temperature.

Fig. 3 shows the variation of XRD patterns for Ba-series as a function of the substitution content after calcined at 1300 °C. $Ba_{0.1}$ sample exhibits only the triclinic structure with a unit cell volume of 350.51 Å^3 compared to 347.91 Å^3 for non-substituted LWO, confirming that Ba^{2+} (1.47 Å) with larger ionic radii than La^{3+} (1.22 Å) [43] forms a solid solution with the triclinic structure, expanding the unit cell. On the other hand, $Ba_{0.15}$ sample fired at 1300 °C shows a mixture of α- and β-polymorphs with cell volumes of 351.85 and 365.07 Å^3 for the triclinic and cubic forms, respectively. Thus, Ba^{2+} is dissolved simultaneously in both phases. Finally, $Ba_{0.2}$ sample exhibits only the cubic phase with cell volume of 366.94 Å^3. A similar trend was found for V-contained samples.

Other substitutions were tested, such as: Sr^{2+}, K^+ and Nb^{5+}. However, they do not stabilise the cubic phase, appearing mixtures of the triclinic form and other stable secondary phases containing the dopant (i.e. $SrWO_4$,

$La_7Nb_3W_4O_{30}$ and K_2WO_4) as illustrated in Fig. 4. These results indicate that only high levels of Ba^{2+} and V^{5+} stabilise the cubic phase at room temperature. Although, high firing temperatures are necessary to avoid secondary phases, such as $BaWO_4$, and to obtain a solid solution. The phase stability for $Ba_{0.2}$ and $V_{0.3}$ was investigated annealing the samples at different temperatures during 1 day. A gradual degradation with the time was observed above 700 °C due to dopant segregation, resulting in a phase transformation from β- to α-polymorph. A similar phenomenon has been observed by Selmi et al. [44] in Ca-substituted $La_2Mo_2O_9$. These authors reported a $\beta \leftrightarrow \alpha$ transformation process in $La_{1.92}Ca_{0.08}Mo_2O_{9-\delta}$ above 640 °C due to calcium segregation.

One should be noted that Mo^{6+} with ionic radii similar to that of W^{6+} stabilises the cubic β-$La_2W_2O_9$ phase without degradation at high temperature [22,25]. This seems to indicate that cation substitutions with ionic radius very different to that of W^{6+}/La^{3+} stabilise the cubic phase in a metastable state. On the other hand, Cr^{6+} (0.44 Å) is other possible substitution in the tungsten site of $La_2W_2O_9$, however Cr^{6+} is easily reduced to Cr^{3+} during the synthesis process above 700 °C and therefore it was not further investigated.

3.2. Structure

The triclinic structure of α-$La_2W_2O_9$ has been reported by Laligant et al. [30] from neutron diffraction data (space group $P\bar{1}$). This structure has isolated $[W_4O_{18}]^{-12}$ groups alternating with trigonal bypiramids generating a 3D framework with lanthanum atoms in both 9- and 10-fold oxygen polyhedra (inset Fig. 5a). The cell parameters obtained by the Rietveld refinement (Fig. 5a) are: $a = 7.2424(2)$ Å, $b = 7.2923(2)$ Å, $c = 7.0469(2)$ Å, $\alpha = 96.393(2)^\circ$, $\beta = 94.699(2)^\circ$ and $\gamma = 70.338(2)^\circ$ and they are in agreement with the literature data [30].

On the other hand, α-$La_2Mo_2O_9$ is a complex structure containing 312 crystallographically independent atoms, which was reported by Evans et al. [7] from single-crystals obtained by spontaneous crystallisation of a melt. This compound was refined as a monoclinic structure (s.g. $P2_1$) with unit cell parameters of: $a = 14.2847(6)$ Å, $b = 21.4533(1)$ Å, $c = 28.6344$ Å and $\beta = 90.442(2)^\circ$. This compound can be described as a $2 \times 3 \times 4$ superstructure relative to the cubic β-polymorph with a slight monoclinic distortion as previously confirmed by electron diffraction studies [2,3,16]. The superstructure and small monoclinic distortion of α-$La_2Mo_2O_9$ is evident in Fig. 5b, where most

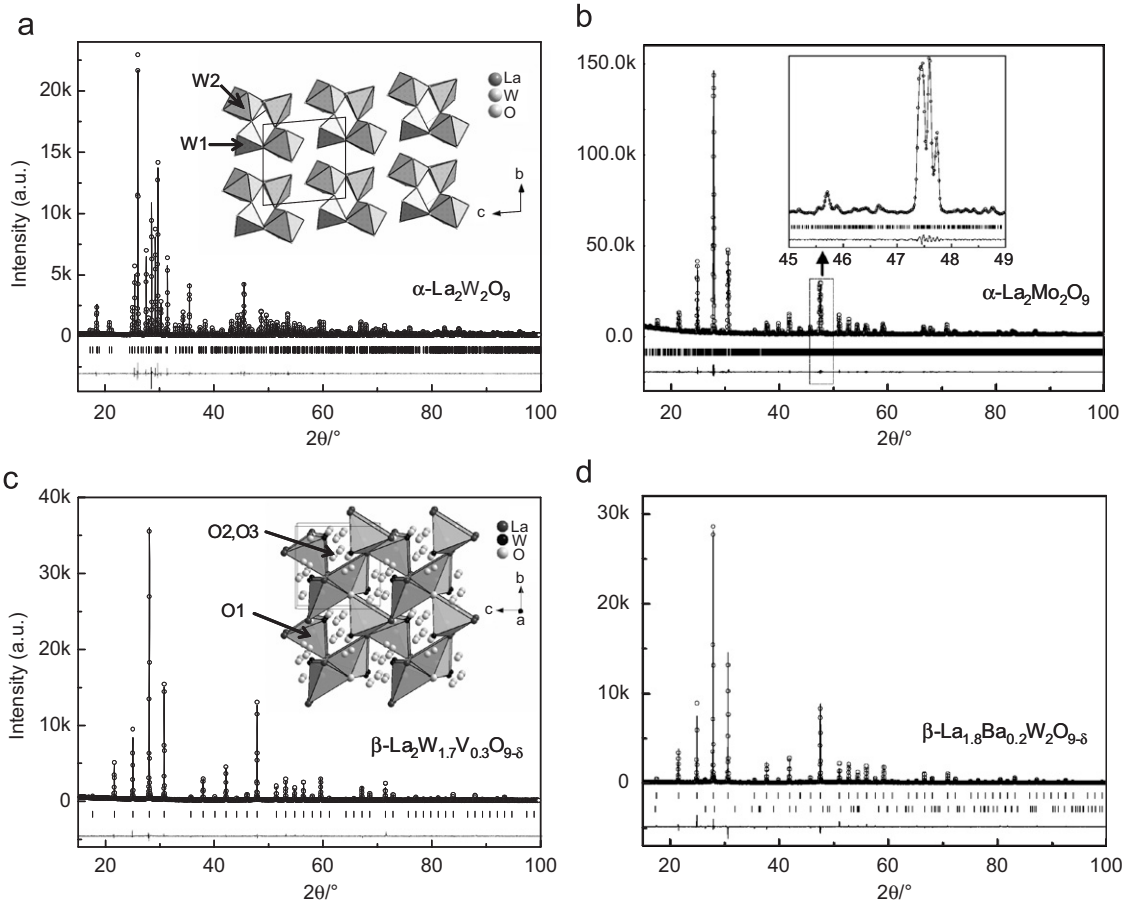

Fig. 5. Rietveld refinement for (a) triclinic α-$La_2W_2O_9$, (b) monoclinic α-$La_2Mo_2O_9$, (c) cubic β-$La_2W_{1.7}V_{0.3}O_{9-\delta}$ and (d) cubic β-$La_{1.8}Ba_{0.2}WO_{9-\delta}$ phases, showing experimental (circles), calculated (continuous line), difference profiles and Bragg positions. The $BaWO_4$ impurity is also refined in (d).

intense diffraction peaks show splitting due to the monoclinic distortion compared to β-$La_2Mo_2O_9$ (Fig. 5c and 5d). Also, small reflections associated to the superstructure can be observed in the background (inset Fig. 5b). Corbel et al. [21] have proposed a new kind of representation for the β-$La_2Mo_2O_9$ structure based on anti-polyhedra. The fully occupied sites in the structure (La, Mo, and O1) form [O1La_3Mo] anti-tetrahedral units around the *O*1 sites. Each anti-tetrahedron shares its three La vertexes with two other anti-tetrahedra to form a 3D rigid framework. Moreover, the *O*2 and *O*3 sites with partial occupation and responsible for the ionic conduction in these materials are located in the channels between anti-tetrahedra (inset Fig. 5c).

The $La_{1.8}Ba_{0.2}W_2O_{9-\delta}$ and $La_2W_{1.7}V_{0.3}O_{9-\delta}$ samples crystallise in a β-structure similar to that of the β-$La_2Mo_2O_9$. The Rietveld refinements were carried out using the models proposed by Goutenoire et al. based on neutron diffraction data [2]. The crystallographic parameters are listed in Table 1 and they are compared with non-substituted β-$La_2Mo_2O_9$ at high temperature. The Rietveld refinement patterns are shown in Fig. 5c and 5d. From the data reported in Table 1, it is evident that the structure of β-$La_2Mo_2O_9$ is similar to that of stabilised β-$La_2W_2O_9$. Even, the final R-factors are also similar (Table 1). It should be noted that $Ba_{0.2}$ sample contains a very small amount of $BaWO_4$ impurity, which is difficult to evaluate. But from Fig. 3, it is clear that Ba-solubility limit in $La_2W_2O_9$ is in the range $0.15<x<0.2$. This solubility limit value is similar to that found for $La_2Mo_2O_9$ [12].

Table 1
Crystallographic parameters for $La_{1.8}Ba_{0.2}W_2O_{9-\delta}$ ($Ba_{0.2}$) and $La_2W_{0.7}V_{0.3}O_{9-\delta}$ ($V_{0.3}$)

	LMO[a]	$V_{0.3}$	$Ba_{0.2}$
a (Å)	7.2192(7)	7.1022(3)	7.1592(5)
La (4*a*)/*A*			
x	0.8535(4)	0.8592(3)	0.8574(3)
B	4.7(1)	3.11(8)	3.76(9)
Occ	1	1	0.90
W (4*a*)/*B*			
x	0.1691(4)	0.1674(3)	0.1646(3)
B	3.6(1)	4.47(9)	5.7(1)
Occ	1	0.85	1
*O*1 (4*a*)			
x	0.323(2)	0.312(2)	0.322(2)
B	8.4(6)	5.5(6)	5.7(6)
Occ	1	1	1
*O*2 (12*a*)			
x	0.969(3)	0.948(4)	0.931(3)
y	0.190(4)	0.219(3)	0.200(4)
z	0.350(4)	0.349(4)	0.337(3)
B	8.4(6)	5.5(6)	5.9(6)
Occ	0.69(1)	0.70(2)	0.70(2)
*O*3 (12*a*)			
x	0.929(5)	0.920(6)	0.8804(6)
y	0.713(4)	0.719(6)	0.685(6)
z	0.520(4)	0.557(6)	0.575(6)
B	8.4(6)	5.5(5)	5.9(6)
Occ	0.44(1)	0.45(2)	0.44(2)
R_{wp} (%)	13.7	12.5	11.3
R_{exp} (%)	6.5	8.8	7.1
R_B (%)	4.3	3.6	7.7

[a]Rietveld refinement at 923 K obtained by high temperature XRD.

3.3. Thermal analysis

The $\alpha \leftrightarrow \beta$ phase transitions for non-substituted LMO and LWO are reversible as can be observed in the DTA curves (Fig. 6a) and also reported in the literature [1,33]. The phase transition temperature for LMO reaches a maximum at 565 °C on heating and the peak is displaced to lower temperature during the cooling ~520 °C (Fig. 6a). In the case of LWO, the phase transition takes place at 1080 °C on heating and a large thermal hysteresis of 125 °C is observed during the heating and cooling processes. The enthalpy change at the phase transition was calculated by numerical integration of the recorded DTA curves after the correction for the calorimetric baseline, taking values of 5.5

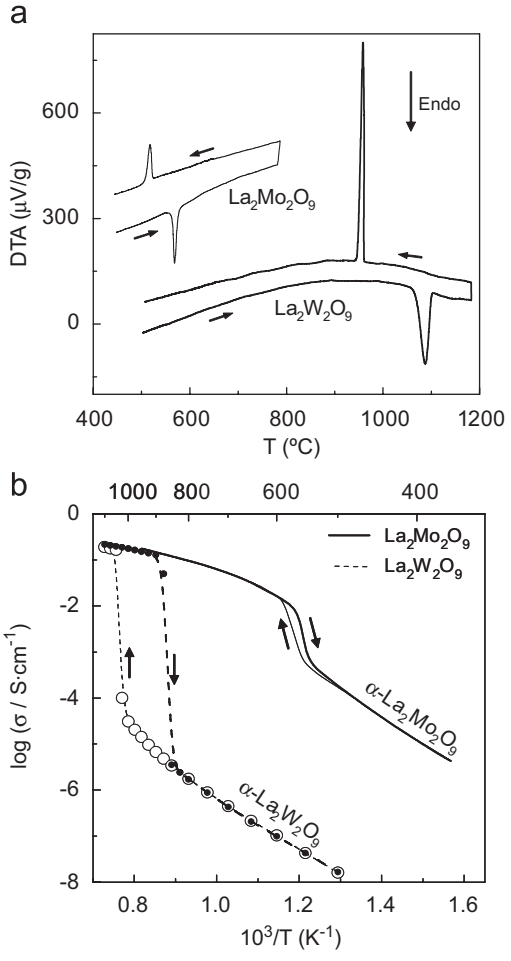

Fig. 6. (a) DTA curves and (b) Arrhenius plot of the overall conductivity for non-substituted $La_2Mo_2O_9$ and $La_2W_2O_9$ during the heating and cooling processes.

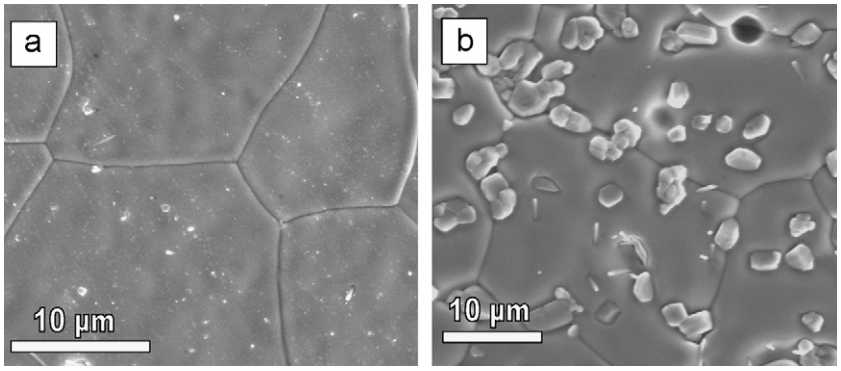

Fig. 7. SEM images for (a) $La_{1.8}Ba_{0.2}W_2O_{9-\delta}$ sample sintered at 1300 °C for 3 h as-prepared and (b) after decomposition at 800 °C for 24 h.

and 27.5 kJ mol^{-1} for LMO and LWO, respectively. The enthalpy change during the triclinic↔cubic transformation for LWO is much higher compared to the pseudocubic↔cubic transformation for LMO, thus supporting the proposed structural interpretation.

The thermal dependence of the overall conductivity for non-substituted $La_2Mo_2O_9$ has been previously studied in several reports [1,34], showing an abrupt enhancement of the conductivity of about one order of magnitude above the phase transition temperature (Fig. 6b). The triclinic α-$La_2W_2O_9$ has lower conductivity values than α-$La_2Mo_2O_9$ in the low temperature range, however the $\alpha \rightarrow \beta$ phase transition for LWO is accompanied by a significant conductivity increase of about four orders of magnitude with similar values to those of β-$La_2Mo_2O_9$. The hysteric behaviour observed during the cooling and heating processes is consistent with the DTA results, which indicates a first order phase transition. As previously mentioned, the stabilisation of the β-$La_2W_2O_9$ polymorph at low temperature would allow to obtain a new series of compounds with ionic conductivity comparable to β-$La_2Mo_2O_9$ and presumably better redox stability due to the absence of molybdenum, which exhibits higher reducibility than tungsten.

3.4. Electrical characterisation

Ceramic pellets sintered at 1300 °C for $V_{0.3}$ and $Ba_{0.2}$ samples have relative density higher than 99%. This high sintering temperature produces a significant grain growth ~20 μm. No phase segregations are observed in sintered samples prepared at 1300 °C and slowly cooled to room temperature (Fig. 7a). However, sintered samples annealed for 24 h above 700 °C show additional particles in the ceramic microstructure with smaller size (Fig. 7b). Such particles were identified as $BaWO_4$ impurities due to phase segregations during the degradation process. The impedance spectra measurements were carried out below 700 °C to avoid structural changes during the experiment. Representative impedance spectra for $Ba_{0.2}$ at 400 and 450 °C are shown in Fig. 8a. The impedance spectra comprise a symmetric and depressed arc with capacitance of ~6 pF cm^{-1}, which is assigned to grain interior (bulk).

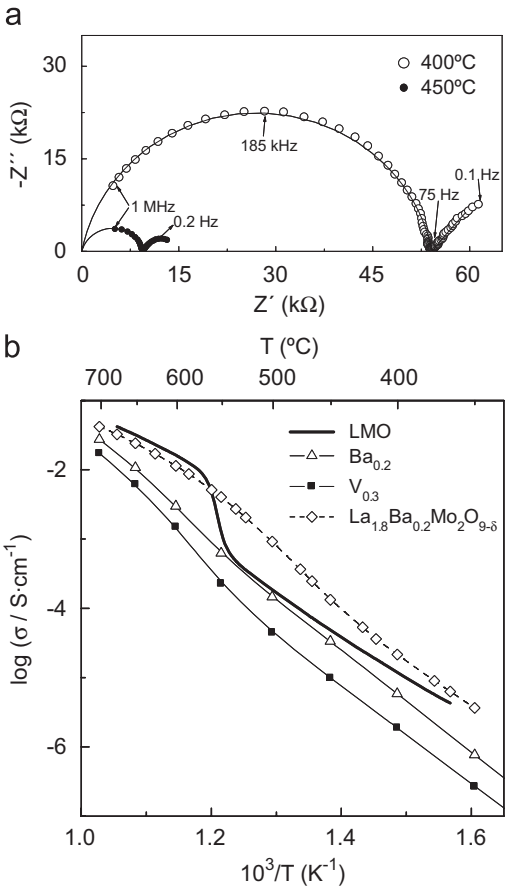

Fig. 8. (a) Impedance spectra for $La_{1.8}Ba_{0.2}W_2O_{9-\delta}$ ($Ba_{0.2}$) sample at 400 and 450 °C. The solid line is the fitting result obtained with equivalent circuits. (b) Arrhenius plot of the overall conductivity for different compositions.

Additionally, the electrode/electrolyte processes are observed at low frequency. The grain boundary process in these samples is negligible, indicating that bulk is the main resistance contribution to the overall conductivity. Fig. 8b compares the Arrhenius plot of the overall conductivity for different samples. $Ba_{0.2}$ and $V_{0.3}$ samples have ionic conductivity lower than LMO in the whole temperature range studied (e.g. 0.011 S cm^{-1} for $Ba_{0.2}$, 0.006 S cm^{-1} for $V_{0.3}$ and 0.032 S cm^{-1} for LMO at 650 °C). In addition, the

molybdate $La_{1.8}Ba_{0.2}Mo_2O_{9-\delta}$ studied in a previous work [12] has comparable conductivity values than those of LMO in the high temperature range and somewhat higher in the low temperature range. The lower conductivity for W-containing samples compared to Mo-containing samples seems to be ascribed to the different cell volume. Thus, a lower cell volume limits the free space for oxygen diffusion and consequently the ionic conductivity decreases. Despite the slightly larger size of W^{6+} compared to Mo^{6+}, the cell parameter of $La_{1.8}Ba_{0.2}Mo_2O_{9-\delta}$ (7.1860 Å) is larger than that of $La_{1.8}Ba_{0.2}W_2O_{9-\delta}$ (7.1592 Å) and the same trend occurs with the conductivity. This behaviour is not common, but it has been previously found in other systems as $BaXO_4$ (X = W and Mo) [45]. In this context, Corbel et al. explained the anomalous contraction in $La_2Mo_{2-y}W_yO_9$ series above $y>0.5$ by a decrease in the coordination number around W [21]. One should be also noted that $Ba_{0.2}$ has higher cell volume than $V_{0.3}$ and the conductivity of the second one is somewhat lower.

3.5. Kinetic of phase transformation

The impedance spectra for dense pellets of $Ba_{0.2}$ annealed at 700 °C as a function of the time are shown in Fig. 9a. As can be observed, the resistance for the bulk contribution increases significantly after several hours due to gradual $\beta\rightarrow\alpha$ transformation. Fig. 9b shows the dependence of the electrical resistance on the annealing time at different isothermal temperatures during the $\beta\rightarrow\alpha$ transformation for $Ba_{0.2}$. This figure indicates that the resistance increases approximately five orders of magnitude during the phase change. It was also observed that increasing the annealing temperature leads to a decrease in time necessary to complete the $\beta\rightarrow\alpha$ transformation. This occurs within 30 h at 700 °C and it is reduced to ~6 h at 800 °C. By contrast $V_{0.3}$ has a better stability at high temperature or alternatively a slow transformation kinetics. Thus, non-decomposition was observed after annealing the ceramic pellets for 2 days at 700 °C, however the complete transformation occurs after annealing at 800 °C for 50 h.

The isothermal transformation $\alpha\rightarrow\beta$ can be studied by the Johnson–Mehl–Avrami (JMA) equation [46,47], which relates the fraction transformed (α) to the time (t) for experiments performed at constant temperature as follows:

$$1-\alpha=\exp[-(Kt)^n] \quad (1)$$

where K is the rate constant and the exponent n is a dimensional parameter, which characterises the morphology of crystal growth. The temperature dependence of the rate constant K could be expressed by an Arrhenius equation:

$$K=K_0\exp\left(-\frac{E_c}{RT}\right) \quad (2)$$

where K_0 is the frequency factor, R is the universal gas constant, T is the annealing temperature and E_c is the activation energy of the transformation process.

In this study, the fraction transformed at different annealing times $\alpha(t)$ was calculated using the relative increase in the electrical conductivity during the phase

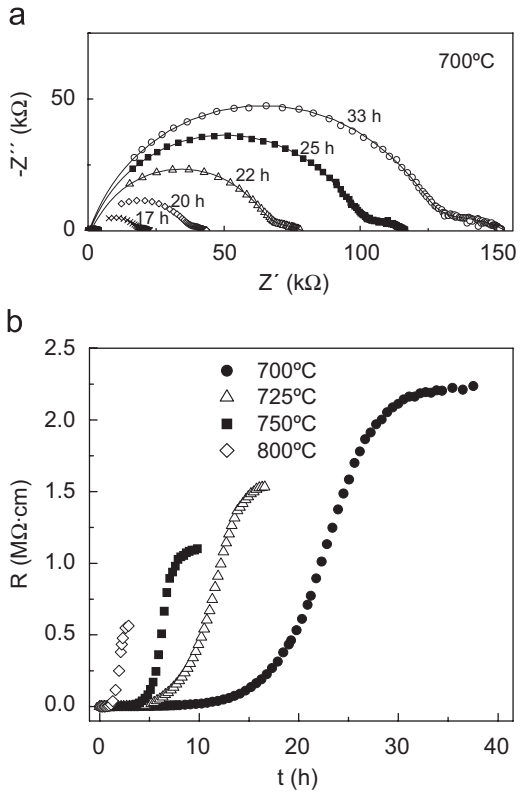

Fig. 9. (a) Impedance spectra for $La_{1.8}Ba_{0.2}W_2O_{9-\delta}$ ($Ba_{0.2}$) sample as a function of the annealing temperature at 700 °C. (b) Time dependence of the overall resistance for $La_{1.8}Ba_{0.2}W_2O_{9-\delta}$ during the $\beta\rightarrow\alpha$ transformation.

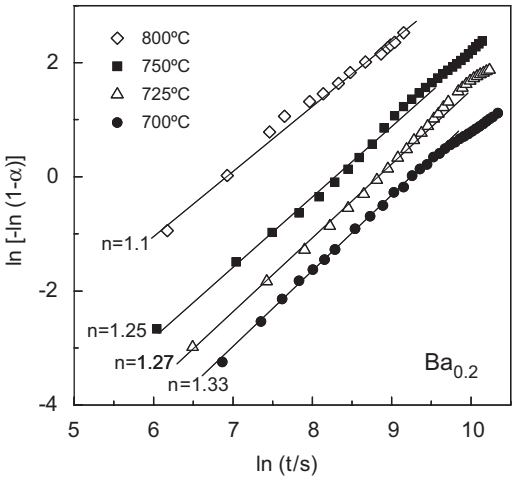

Fig. 10. Avrami plot for the isothermal transformation $\beta\rightarrow\alpha$ for $La_{1.8}Ba_{0.2}W_2O_{9-\delta}$ ($Ba_{0.2}$) at different annealing temperatures.

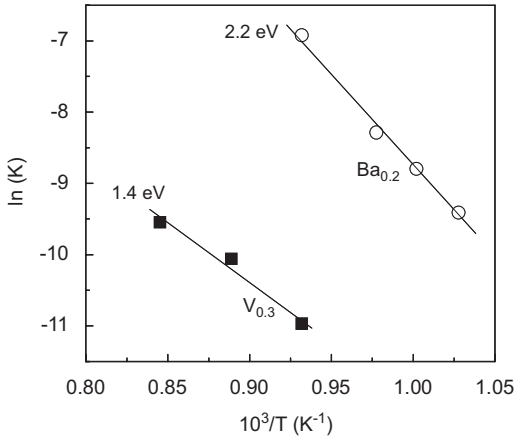

Fig. 11. Arrhenius plots of the $\beta \rightarrow \alpha$ phase transformation for $Ba_{0.2}$ and $V_{0.3}$ samples.

transformation from the following empirical relation [48,49]:

$$\alpha(t) = \frac{\sigma_e - \sigma(t)}{\sigma_e - \sigma_b} \quad (3)$$

where σ_b and σ_e are the respective conductivities at the beginning and the end of the transformation process and $\sigma(t)$ is the conductivity at time t between these two limits. The Avrami plot indicates that the transformation occurs mainly in a single stage, though a slight slope change is observed for high transformed fraction (Fig. 10). The isothermal kinetic parameter n varies from 1.3 to 1.1 with increasing temperature, indicating that the transformation takes place with predominance of homogeneous nucleation and one-dimensional growth. The activation energy of the transformation process was calculated using the Arrhenius representation from Eq. (2). Fig. 11 shows the Arrhenius plots for $Ba_{0.2}$ and $V_{0.3}$ samples, where the activation energy takes values of 2.2 eV for $Ba_{0.2}$ and 1.4 eV for $V_{0.3}$ samples.

4. Conclusions

A substitution strategy was used to stabilise the β-$La_2W_2O_9$ phase at room temperature and to obtain new tungstate electrolytes with LAMOX-type structure. Several substitution were tested, i.e. La^{3+} by Ba^{2+}, Sr^{2+} and K^+; and W^{6+} by V^{5+} and Nb^{5+}. Nanocrystalline materials prepared by freeze-drying precursor retained the cubic phase at room temperature, although the bulk triclinic phase is recovered when the temperature increases and the crystallite size grows. Only high levels of Ba^{2+} and V^{5+} substitution retained the cubic form at room temperature after heating at 1300 °C. However, these materials are metastable above 700 °C, experimenting a gradual transformation from the cubic β-phase to the triclinic α-phase due to phase segregations. The transformation kinetic of $\beta \rightarrow \alpha$ degradation was studied from the time dependence of the overall conductivity in samples annealed above 700 °C. Ba-containing samples are less stable than V-containing samples. The electrical measurements indicated that molybdates with LAMOX-type structure exhibit higher conductivity than tungstates. The reason seems to be associated to the lower unit cell volume of tungsten containing samples, which reduces the free space for oxygen diffusion and hence decreasing the conductivity.

Acknowledgments

This work was supported by the Spanish Research program (MAT2004-3856). The authors wish to thank "Programa de Incorporación de doctores y tecnólogos a empresas privadas y otras entidades", (D. M.-L.) and "Ministerio de Educación y Ciencia" for a "Ramón y Cajal" fellowship (J. C. R.-M.).

References

[1] P. Lacorre, F. Goutenoire, O. Bohnke, R. Retoux, Y. Laligant, Nature 404 (2000) 856.
[2] F. Goutenoire, O. Isnard, R. Retoux, P. Lacorre, Chem. Mater. 12 (2000) 2575.
[3] F. Goutenoire, O. Isnard, R. Retoux, O. Bohnke, Y. Laligant, P. Lacorre, J. Mater. Chem. 11 (2001) 119.
[4] M. Mogensen, N.M. Sammes, G.A. Tompsett, Solid State Ionics 129 (2000) 63.
[5] N.Q. Minh, T. Takahashi, Science and Technology of Ceramic Fuel Cell, Elsevier, NY, 1995.
[6] B.C.H. Steele, A. Heinzel, Nature 414 (2001) 345.
[7] I.R. Evans, J.A.K. Howard, J.S.O. Evans, Chem. Mater. 17 (2005) 4074.
[8] Q.F. Fang, X.P. Wang, Z.S. Li, G.G. Zhang, Z.G. Yi, Mater. Sci. Eng. A 370 (2004) 365.
[9] X.P. Wang, Q.F. Fang, Solid State Ionics 146 (2002) 185.
[10] R. Subasri, D. Matusch, H. Näfe, F. Aldinger, J. Eur. Ceram. Soc. 24 (2004) 129.
[11] S. Basu, P.S. Devi, H.S. Maiti, Appl. Phys. Lett. 85 (2004) 3486.
[12] D. Marrero-López, D. Pérez-Coll, J.C. Ruiz-Morales, J. Canales-Vázquez, M.C. Martín-Sedeño, P. Núñez, Electrochim. Acta 52 (2007) 5219.
[13] X.P. Wang, Z.J. Cheng, Q.F. Fang, Solid State Ionics 176 (2005) 761.
[14] S. Georges, F. Goutenoire, F. Altorfer, D. Sheptyakov, F. Fauth, E. Suard, P. Lacorre, Solid State Ionics 161 (2003) 231.
[15] S. Georges, F. Goutenoire, P. Lacorre, M.C. Steil, J. Eur. Ceram. Soc. 25 (2005) 3619.
[16] D. Marrero-López, J. Canales-Vázquez, W. Zhou, J.T.S. Irvine, P. Núñez, J. Solid State Chem. 179 (2006) 278.
[17] D. Marrero-López, P. Núñez, M. Abril, V. Lavín, U.R. Rodríguez-Mendoza, V.D. Rodríguez, J. Non-Cryst. Solids 345–346 (2004) 377.
[18] Z.S. Khadasheva, N.U. Venskovskii, M.G. Safronenko, A.V. Mosunov, E.D. Politova, S.Y. Stefanovich, Inorg. Mater. 38 (2002) 1168.
[19] S. Basu, P.S. Devi, H.S. Maiti, J. Electrochem. Soc. 152 (2005) A2143.
[20] C. Li, X.P. Wang, J.X. Wang, D. Li, Z. Zhuang, Q.F. Fang, Mater. Res. Bull. 42 (2007) 1077.
[21] G. Corbel, Y. Laligant, F. Goutenoire, E. Suard, P. Lacorre, Chem. Mater. 17 (2005) 4678.
[22] J. Collado, M.A.G. Aranda, A. Cabeza, P. Olivera-Pastor, S. Bruque, J. Solid State Chem. 167 (2002) 80.
[23] X.P. Wang, D. Li, Q.F. Fang, Z.J. Cheng, G. Corbel, P. Lacorre, Appl. Phys. Lett. 89 (2006) 021904-1.
[24] S. Georges, F. Goutenoire, Y. Laligant, P. Lacorre, J. Mater. Chem. 13 (2003) 2317.

[25] D. Marrero-López, J. Canales-Vázquez, J.C. Ruiz-Morales, J.T.S. Irvine, P. Núñez, Electrochim. Acta 50 (2005) 4385.
[26] P. Pinet, J. Fouletier, S. Georges, Mater. Res. Bull. 42 (2007) 935.
[27] R. Subasri, H. Näfe, F. Aldinger, Mater. Res. Bull. 38 (2003) 1965.
[28] D. Marrero-López, J.C. Ruiz-Morales, D. Pérez-Coll, P. Núñez, J.C.C. Abrantes, J.R. Frade, J. Solid State Electrochem. 8 (2004) 638.
[29] A. Tarancon, T. Norby, G. Dezanneau, A. Morata, F. Peiró, J.R. Morante, Electrochem. Solid State Lett. 7 (2004) A373.
[30] Y. Laligant, A. Le Bail, F. Goutemoire, J. Solid State Chem. 159 (2001) 223.
[31] T.-Y. Jin, M.V. Madhava Rao, C.-L. Cheng, D.-S. Tsai, M.-H. Hung, Solid State Ionics 178 (2007) 367.
[32] D. Marrero-López, J. Peña-Martínez, J.C. Ruiz-Morales, D. Pérez-Coll, M.C. Martín-Sedeño, P. Núñez, Solid State Ionics 178 (2007) 1366.
[33] M. Yoshimura, A. Rouanet, Mater. Res. Bull. 11 (1976) 151.
[34] D. Marrero López, J.C. Ruiz-Morales, P. Núñez, J.C.C. Abrantes, J.R. Frade, J. Solid State Chem. 177 (2004) 2378.
[35] D. Marrero-López, J. Canales-Vázquez, J.C. Ruiz-Morales, A. Rodríguez, J.T.S. Irvine, P. Núñez, Solid State Ionics 176 (2005) 1807.
[36] D. Marrero-López, J. Peña-Martínez, D. Pérez-Coll, P. Núñez, J. Alloys Compd. 422 (2006) 249.
[37] J. Rodríguez-Carvajal, Phys. B: Condens. Matter 192 (1993) 55.
[38] T. Roisnel, J. Rodríguez-Carvajal, WinPLOTR, Laboratoire Léon Brillouin-LCSI, France, 2005.
[39] D. Johnson, ZView: a Software Program for IES Analysis, Version 2.8, Scribner Associates, Inc., 2005.
[40] C. Garvie, J. Phys. Chem. 69 (1965) 1238.
[41] H. Gleiter, Prog. Mater. Sci. 33 (1989) 223.
[42] K. Lu, Y.H. Zhao, Nanostruct. Mater. 12 (1999) 559.
[43] R.D. Shannon, C.T. Prewitt, Acta Crystallogr. A32 (1976) 751.
[44] A. Selmi, G. Corbel, P. Lacorre, Solid State Ionics 177 (2006) 3051.
[45] T.I. Bylichkina, L.I. Soleva, E.A. Pobedimskaya, M.A. Porai-Koshifts, N.V. Belov, Kristallografiya 15 (1970) 165.
[46] M. Avrami, J. Chem. Phys. 9 (1941) 177.
[47] W.A. Johnson, K.F. Mehl, Trans. Am. Inst. Min. Metall. Eng. 135 (1932) 416.
[48] M.F. Kotkata, M.-K. El-Mously, S.A. Salam, J. Phys. C 11 (1978) 1077.
[49] M.F. Kotkata, A.F. El-Dib, Mater. Sci. Eng. 72 (1985) 163.